

Direct ultrafast carrier imaging in a perovskite microlaser with optical coherence microscopy

MAXIM A. SIROTIN,¹ ANNA A. POPKOVA,¹  VLADIMIR O. BESSONOV,¹  IRINA V. SOBOLEVA,¹ EVGENY V. LYUBIN,¹ ANATOLY P. PUSHKAREV,² SERGEY V. MAKAROV,^{2,3} AND ANDREY A. FEDYANIN^{1,*} 

¹Faculty of Physics, Lomonosov Moscow State University, Moscow 119991, Russia

²School of Physics and Engineering, ITMO University, St. Petersburg 197101, Russia

³Qingdao Innovation and Development Center, Harbin Engineering University, Qingdao 266000, Shandong, China

*fedyanin@nanolab.phys.msu.ru

Received 28 June 2023; revised 6 September 2023; accepted 12 September 2023; published 6 October 2023

Nanophotonics is an actively developing field of optics that finds application in various areas, from biosensing to quantum computing. The study of ultrafast modulation of the refractive index Δn is an important task in nanophotonics, since it reveals the features of light–matter interaction inside devices. With the development of active photonic devices such as emitters and modulators, there is a growing need for Δn imaging techniques with both high spatial and high temporal resolutions. Here, we report on an all-optical ultrafast Δn imaging method based on phase-sensitive optical coherence microscopy with a resolution of 1 ps in time and 0.5 μm in space and a sensitivity to Δn down to 10^{-3} RIU. The advantages of the method are demonstrated on emerging nanophotonic devices—perovskite microlasers, in which the ultrafast spatiotemporal dynamics of the refractive index during lasing is quantitatively visualized, illustrating the features of relaxation and diffusion of carriers in perovskites. The developed method allows us to estimate the ultrafast carrier diffusion and relaxation constants simultaneously and to show that the CsPbBr₃ perovskite carrier diffusion coefficient is low compared to other semiconductors even during lasing at high carrier densities, which leads to high localization of the generated carrier cloud, and, consequently, to high fluorescence and lasing efficiency. The resulting technique is a versatile method for studying ultrafast carrier transport via Δn imaging, paving an avenue for the applications of optical coherence tomography and microscopy in the research of nanophotonic devices and materials. © 2023

Optica Publishing Group under the terms of the [Optica Open Access Publishing Agreement](#)

<https://doi.org/10.1364/OPTICA.498746>

1. INTRODUCTION

The development of nanophotonics leads to the emergence of new types of optical signal sources, detectors, and modulators [1,2]. With the increasing complexity of active optical devices, there is a need to adapt existing methods and create new ones for local characterization of the light–matter interaction. Nonlinear [3] and near-field [4,5] microscopy can be considered to map the optical fields in nanostructures, while fluorescence-lifetime imaging microscopy (FLIM) [6], transient reflection/absorption techniques [7,8], and ultrafast perturbation mapping [9,10] provide information about the generation and dynamics of free carriers in nanophotonic devices. However, many of these methods have limitations in quantifying carrier concentration and simultaneously achieving high temporal and spatial resolutions, which restricts their use in such cases where estimation of carrier diffusion on picosecond scales is crucial (e.g., microlasers, micro-modulators, etc.).

Various techniques based on ultrafast electron microscopy with sub-picosecond time resolution and nanoscale space resolution

have also been developed to improve the spatial resolution in imaging [11,12]. However, electron microscopy methods are difficult to implement on an optical table and sophisticated to combine with optical measurements. Therefore, it is important to develop a novel all-optical technique for ultrafast characterization of micro- and nanoscale optical devices.

The free carriers generated directly affect the material's refractive index, resulting in the addition of Δn , the distribution of which could provide information about the concentration and spreading of carriers. A powerful method for studying the spatial distribution of the refractive index is optical coherence tomography (OCT), which has revolutionized the field of biomedical imaging [13,14]. A variation of OCT, optical coherence microscopy (OCM), inherits high interference phase sensitivity and quantitative refractive index measurements from OCT and high transverse resolution from confocal microscopy [13–20]. OCT and OCM have already shown their promise for noninvasive visualization of the internal structure of 3D-printed microstructures [21–23] and integrated nanophotonic passive devices [24,25]. The use of supercontinuum pulses from femtosecond lasers as a

radiation source [26–28] allows measurements to be carried out in the ultrafast probe–pump scheme, making OCM an excellent basis for the development of ultrafast Δn imaging techniques in nanophotonics. Previously, the pump–probe OCT was only used for molecular contrast imaging at nanosecond timescales [29,30].

Here, we succeeded in implementing the pump–probe scheme with picosecond probe pulses performing OCM. We tested our method on perovskite microlasers, which exhibit high efficiency at room temperature and a wide tuning range, and can be fabricated by low-cost solution-processible methods [31–38]. The efficiency of perovskite microlasers is significantly affected by the density of generated charge carriers, as well as the relaxation processes and the transport of charge carriers related to the crystal structure and its defects [6,36,39]. Carrier dynamics in perovskites is often studied using a transient reflection/absorption method [40–43], which has a femtosecond resolution, usually without giving a spatial picture of the processes and suffering from probe radiation interference inside the sample [44]. Temporally resolved photoluminescence spectroscopy [34,42,45–47] shows the lasing spectral–temporal dynamics without spatial resolution or quantitative carrier information. FLIM [6] has a submicrometer transverse resolution, but is limited by a subnanosecond temporal resolution. However, studying the relaxation of carriers during lasing in perovskites requires picosecond temporal resolution, because the characteristic relaxation times of free carriers through stimulated emission are from 1 ps to 20 ps, while spontaneous ones are from 100 ps to 500 ps upon excitation by femtosecond pulses [42,45,48].

In this work, we develop a novel scheme for pump–probe OCM to register modulation in the refractive index with the resolution of 1 ps in time, 0.5 μm in space, and a sensitivity of down to 10^{-3} RIU, improving the previously achieved OCT/OCM temporal resolution by three orders of magnitude. Direct quantitative spatiotemporal visualization of the dynamics of carriers in a perovskite crystal during lasing is carried out, and the relaxation and diffusion constants are estimated simultaneously. The resulting

technique is a versatile method for studying ultrafast carrier transport and Δn imaging, paving a new avenue for OCT and OCM applications in the research of nanophotonic devices and materials.

2. METHODS

A. Experimental Setup

The experimental setup implements a pump–probe scheme with OCM as the probe (Fig. 1). Figure 1(b) illustrates the schematic of the developed method, where the pump beam is indicated by green lines and the OCM beams are indicated by red lines. Figure 1(c) shows the data acquisition process.

The femtosecond laser (Avesta TEMA) with the center wavelength of 1050 nm, an average power of 3.5 W, a pulse duration of 100 fs (spectrum width of 13 nm), a pulse energy of 50 nJ, and a repetition rate of 70 MHz is used as a source. The source radiation passes through a pulse picker which reduces the pulse repetition rate to 50 kHz to avoid sample overheating. Next, the second harmonic of the source radiation is generated in a nonlinear crystal (β -barium borate, BBO) and is used as a pump. A part of unconverted source radiation is coupled into a nonlinear photonic crystal fiber (PCF, NKT Photonics SC-5.0-1040), in which a supercontinuum radiation (SC) with a wide spectrum from 925 nm to 1125 nm is generated for the OCM probe based on the Michelson interferometer. The probe pulse duration is 5 ps due to chirping in PCF; a special algorithm was applied to improve the temporal resolution down to 1 ps (see Supplement 1, Section 1 for details). The position of the reference mirror (RM) of the interferometer is chosen to provide pronounced interference between the reference and signal beams, which corresponds to a path difference of approximately 10 μm to 20 μm [14]. The probe beam scans the sample with galvanic mirrors (GM), which makes it possible to construct the spatial distribution of the refractive index at the fixed pump beam position.

The pump beam passes through a delay line based on the linear translation stage (OptoSigma OSMS26-300), providing temporal scanning in the range of 2 ns with a minimum step of 30 fs (note

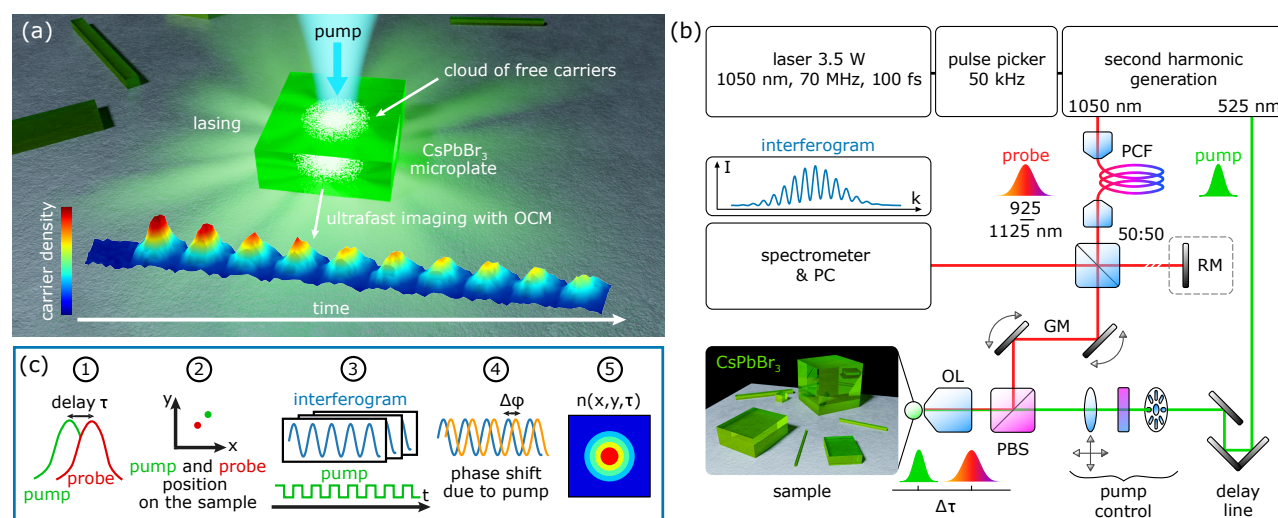


Fig. 1. (a) Sketch of the experiment. A pump beam generates the cloud of free carriers in the perovskite microplate, causing lasing. At zero time delay, the free carrier cloud profile coincides with the pump beam intensity profile. The spatiotemporal dynamics of the carrier cloud is visualized using ultrafast OCM. Here, the pump beam is shown in bluish color for clarity. (b) Schematic of the pump–probe OCM setup. OL, objective lens; PBS, polarizing beam splitter; PCF, photonic crystal fiber for supercontinuum generation; RM, reference mirror (not needed in common-path OCM); GM galvanometer-mounted mirror. Pump control: optical chopper, liquid crystal retarder, and steering lens. (c) Data acquisition algorithm.

that the time resolution is 1 ps due to the probe pulse width). Pump control includes an optical chopper and a liquid crystal retarder for power tuning and a steering lens for pump beam positioning. The chopper modulates the pump to further separate the signal against the noise background, the retarder together with the polarization beam splitter (PBS) performs automatic adjustment of the pump power, and the steering lens changes the position of the beam spot and its size in the sample area.

The pump and probe beams are aligned with a PBS and focused on the sample using a high-numerical-aperture (NA) objective lens (LOMO, NA = 0.85, 40×). The waist radii are 2.25 μm and 0.5 μm at 1/e² level for pump and probe beams, respectively. Modulation in the refractive index of the sample induced by the pump beam changes the optical path of the probe beam, which is reflected from the sample and interferes with the OCM reference beam. The spectrum resulting from the interference is recorded by the spectrometer (Ocean Optics QE Pro, 400–1150 nm range, 1.5 nm resolution). The interference manifests itself as a cosine wave superimposed on the wide supercontinuum spectrum. The refractive index changes induced in the sample can be calculated from the interference pattern using the fast Fourier transform (FFT). If the sample with 0.5–5 μm thickness is illuminated from below, the beams reflected from the upper and lower surfaces of the sample act as a signal and reference, respectively, and the RM is not needed. In this case, the signal beam passes through the region of the modulated refractive index Δn , while the reference beam reflects from the lower boundary and therefore does not interact with the Δn region. The perovskite crystal samples were studied in this configuration, called common-path OCM [18], since it is more noise tolerant. For the sample with <0.5 μm or >5 μm thickness, the common-path OCM configuration is not suitable, and the RM is needed (as for a sample of a silicon waveguide in Supplement 1, Section 5 or in Ref. [25]). The lower limit of the suitable sample thickness for a common-path OCM configuration is determined by the width of the OCM spectrum (the wider the spectrum, the thinner the samples that can be examined), while the upper limit is determined by the signal collection depth, which is affected by the lens focus depth and confocal gating [14,18].

B. Data Acquisition Algorithm

The data acquisition algorithm consisting of five stages is shown in Fig. 1(c). (1) The time delay between the pump and probe pulses (τ) is set by positioning the delay line retroreflection mirrors. (2) The positions of the pump and probe beams on the sample are aligned using a steering lens and galvanic mirrors, respectively. (3) The pump pulse affects the refractive index of the sample, which changes the optical path of the signal pulse in the OCM and modifies the interference pattern. The spectrometer takes interferograms with an exposure time of 8 ms. To reduce the noise, the registration is performed in the lock-in mode: the pump beam is modulated (open–close) by an optical chopper with a frequency of 20 Hz (50 ms period, six interferograms per period), and the spectral signal is registered at the chopper frequency. (4) The interferogram is processed by computer software. The spectrum is normalized to an interference-free spectrum, and the Fourier phase is extracted. Then the changes in the amplitude of the Fourier phase ($\Delta\varphi$) at the chopper frequency are determined [20]. The $\Delta\varphi$ carries information about the modulation in the optical path and refractive index Δn in the sample under the action of the pump pulse. (5) Measurements in stages 1–4 are repeated for various time

delays τ and different positions (x, y) of the probe beam on the sample. By varying τ, x, y , one can obtain a map of modulation in the refractive index $\Delta n(\tau, x, y)$ with a spatial resolution of 0.5 μm and a temporal resolution of 1 ps, which forms the basis of the experimental data.

The configuration of the experiment makes it possible to record simultaneously the fluorescence spectra of the sample and changes in its refractive index using the same spectrometer.

C. Samples

To demonstrate the capabilities of the developed technique, perovskite microlasers were chosen. The perovskites have a high refractive index, which significantly changes under the action of free carrier generation. On the other hand, the spatiotemporal dynamics of carriers affects the efficiency of laser generation and the quantum yield of fluorescence [6,36,39]. Laser generation in perovskite microcrystals can be caused by a femtosecond pump pulse illuminating either the entire sample or part of it [38]. This enables us to study the spatial dynamics of a locally generated plasma cloud during lasing.

The samples under study were CsPbBr₃ perovskite microcrystals grown by the method of rapid precipitation from dimethyl sulfoxide solution sprayed onto hydrophobic substrates at ambient conditions on a 0.17 mm thick glass substrate (for details on synthesis protocol, see elsewhere [49]), which makes it possible to achieve monocrystalline structures with a low concentration of defect states [49–51]. The sample contains large crystals, microplates (crystals with a length and width of 5–10 μm and a height of 0.5–2 μm), and nanostrips (narrow crystals several micrometers long), as shown in Fig. 1(b). Microplates were chosen as representative samples, since unlike large crystals, lasing can occur in them, and unlike nanostrips, a map of Δn can be visualized along both the x and y directions during lasing. A microplate with a size of ($L \times W \times H$) $8 \times 8 \times 1.5 \mu\text{m}^3$ was chosen as the main sample [Fig. 2(a), upper inset], and the exact size was determined using atomic force microscopy (AFM).

3. RESULTS AND DISCUSSION

The main mechanism of laser generation in lead halide perovskite microplates under ultrafast optical pumping is the stimulated emission of the electron–hole plasma (EHP) [42,45]. The contribution of carrier density N_{EHP} to the complex permittivity $\varepsilon(\omega)$ (dielectric function) is described by the Lorentz model [52–54]

$$\varepsilon(\omega) = [n(\omega) + ik(\omega)]^2 = \varepsilon_b \left(1 + \frac{\omega_p^2}{\omega_0^2 - \omega^2 - i\Gamma\omega} \right), \quad (1)$$

where $\omega_p^2 = \frac{e^2 N_{\text{EHP}}}{m^* \varepsilon_0}$ is the plasma frequency, ε_b is the background dielectric constant, ω_0 is the band gap frequency, Γ is the dephasing rate, m^* is the effective mass of the electron [55], e is the elementary charge, and ε_0 is the vacuum permittivity.

The form of the spectral dependence of the EHP-induced addition Δn to the refractive index obtained from Eq. (1) for CsPbBr₃ perovskite at a concentration of $N_{\text{EHP}} = 1.1 \cdot 10^{19} \text{ cm}^{-3}$ is shown in Fig. 2(a) (bottom inset). The pump and probe wavelengths used in the experiment are marked with red and green bands, respectively. For probe wavelengths away from the resonance (as in our case), the refractive index modulation Δn depends linearly on

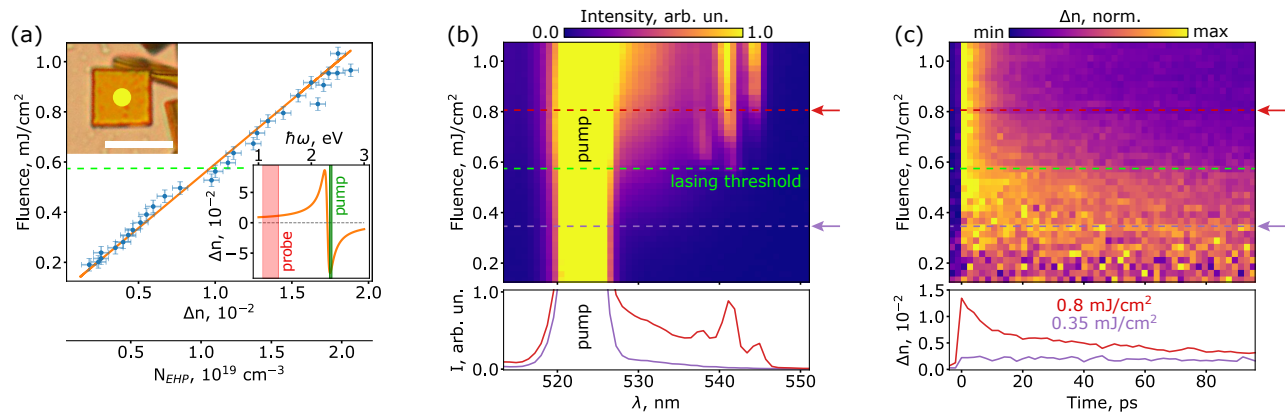


Fig. 2. Spectral–temporal characterization of the perovskite sample with pump and probe beams focused at the center of the sample. (a) Dependence of the refractive index modulation Δn (and, accordingly, the concentration of electron–hole plasma N_{EHP}) versus the pump fluence. The top inset shows an optical transmission microscope image of the crystal. The yellow dot shows the position and diameter of the pump beam. Scale bar is 10 μm . The lower inset illustrates $\Delta n(\omega)$ from Eq. (1) with $N_{\text{EHP}} = 1.1 \cdot 10^{19} \text{ cm}^{-3}$, the green line denotes pump, and the red band is the spectrum of the probe. (b) Dependence of the fluorescence spectrum of the sample on the pump fluence. (c) Dependence of the relaxation dynamics of the refractive index modulation on the pump fluence (each horizontal line corresponding to a certain fluence value is normalized to the maximum Δn value in the line). The green dashed lines mark the lasing threshold, and the red and purple dashed lines indicate fluences, for which the spectra (b) and non-normalized kinetic curves (c) are shown in the bottom subplots.

the plasma concentration N_{EHP} (see Supplement 1, Section 2 for details). At long wavelengths $\omega \rightarrow 0$, and while $\omega_p \ll \omega_0$, Δn can be estimated from the asymptotic formula

$$N_{\text{EHP}} \approx \frac{2\omega_0^2 m^* \varepsilon_0}{\sqrt{\varepsilon_b} e^2} \Delta n. \quad (2)$$

Below the saturation, the number of generated carriers is proportional to the pump intensity [45,56]. Thus a linear dependence of Δn and N_{EHP} on the pump fluence is expected at probe wavelengths.

In the experiment, the microplate sample was excited with focused pump radiation (waist radius is 2.25 μm at $1/e^2$ level) located at the center of the sample [Fig. 2(a), top inset; a yellow circle marks the pump position]. Figure 2(a) shows the dependence of Δn on the pump fluence measured at zero time delay between the pump and probe. The dependence is linear, which is in excellent agreement with the Lorentz model described above. An additional scale on the x axis converts Δn to the concentration of free carriers according to Eq. (1). The linear relationship between Δn and the carrier concentration is an advantage for the method allowing quantitative imaging of electron–hole plasma clouds.

To register lasing in the perovskite microcrystal and to determine the lasing threshold, the perovskite fluorescence spectra were recorded for various pump fluences [Fig. 2(b)]. Only a broad band of luminescence is observed in the spectra up to the fluence of 0.57 mJ/cm², which is clearly visible even despite the close pump line. As the fluence exceeds 0.57 mJ/cm², a narrow lasing line appears. Therefore, we will consider this value to be the lasing threshold pump fluence. With a further increase in fluence, the appearance of additional lasing modes and the transfer of energy between them are observed, which is associated with the red shift of the lasing gain profile and band gap renormalization [45]. In addition, a small blue shift for specific modes can be observed in Fig. 2(b), which is caused by a change in the refractive index of the material [34,42,45,47].

Overcoming the threshold fluence is accompanied not only by the appearance of lasing lines in the fluorescence spectrum,

but also by the change in the nature of the ultrafast dynamics of Δn , and, consequently, ultrafast dynamics of the plasma N_{EHP} [Fig. 2(c)]. In the experiment, we have simultaneously recorded the fluorescence spectra and the sample Δn as a function of the time delay between the pump and probe pulses. At fluences below the threshold, the Δn dynamics exhibits slow relaxation, while at fluences above, a fast component appears, associated with lasing (stimulated emission).

It should be noted that the rapid relaxation of conductivity and Δn in semiconductor crystals can also be associated with the formation of excitons from unbound electrons and holes in plasma even at room temperature [57]. However, in this work, the carrier density ($N \sim 10^{19} \text{ cm}^{-3}$) is higher than the Mott density ($N_{\text{Mott}} \sim 10^{17} \text{ cm}^{-3}$) [45], the appearance of the fast relaxation component Δn is accompanied by the simultaneous appearance of lasing lines (indicating stimulated carrier relaxation), and a plasma red shift of the lasing gain profile is also observed, which speaks in favor of predominantly plasma carriers and EHP-dependent Δn [42,45].

Since Δn is directly proportional to N_{EHP} , the dynamics of Δn immediately gives the information about the carrier dynamics. Up to the threshold value, the main mechanism of carrier relaxation is spontaneous emission, characterized by relaxation times of the order of 100 ps [34,45]. Above the threshold value, the greatest contribution is made by stimulated emission with characteristic relaxation times from 8 ps to 20 ps [34,45]. Thus, the lasing threshold can be determined not only by the appearance of lasing lines in the fluorescence spectrum of the sample, but also by the occurrence of a fast component in the dynamics of the refractive index, associated with the transition from spontaneous to stimulated emission.

Comparison of Figs. 2(a)–2(c) allows estimating Δn and N_{EHP} corresponding to the lasing threshold: $\Delta n^{\text{th}} = 1 \cdot 10^{-2}$, $N_{\text{EHP}}^{\text{th}} = 1.1 \cdot 10^{19} \text{ cm}^{-3}$. The use of asymptotic Eq. (2) makes it possible to estimate the threshold concentration as $N_{\text{EHP}}^{\text{th}} = 1.5 \cdot 10^{19} \text{ cm}^{-3}$, which overestimates the value by only

Table 1. Comparison of Measured Perovskite Microlaser Parameters with Literature Data for Various Lead Halide Perovskite Samples^a

Parameter	This Work	Previous Works
$A, 10^8 \text{ s}^{-1}$	2	1–20 [6,58]
$B, 10^{-9} \text{ cm}^3/\text{s}$	1.8	0.03–2.4 [6,58]
$C, 10^{-29} \text{ cm}^6/\text{s}$	≤ 1	0.5 [58]
τ_{lasing}	13 ps	5 ps [59]–80 ps [46]
τ_{fluor}	170 ps	175 ps [45]–7.2 ns [60]
$D, \text{ cm}^2/\text{s}$	≤ 1	0.55 [6]–1.1 [61]
$N^{\text{th}}, \text{ cm}^{-3}$	$1.1 \cdot 10^{19}$	$1.5 \cdot 10^{16}$ [34,45]– $7.9 \cdot 10^{19}$
$\Delta n^{\text{th}} (\lambda = 1050 \text{ nm})$	$1 \cdot 10^{-2}$	—

^aHere, D is the carrier diffusion coefficient, N^{th} is the lasing threshold carrier density, and Δn^{th} is the refractive index modulation corresponding to the lasing threshold carrier density. Carriers can be both excitons [34] (exciton lasing) and electron–hole plasma [42,45] (EHP lasing).

40% compared to the original Eq. (1). Threshold carrier concentrations have been reported ranging from $1.5 \cdot 10^{16} \text{ cm}^{-3}$ for low-threshold nanowires in the exciton lasing mode [34] to $7.9 \cdot 10^{19} \text{ cm}^{-3}$ for 10–20 μm CsPbBr₃ microplate lasers in the electron–hole plasma lasing mode [45] (Table 1). Our data are in good agreement with the latter value, which indicates the applicability of the method for quantitative imaging of carriers.

The lasing threshold value of perovskite microlasers strongly depends on many factors, such as the chemical composition of samples, fabrication process, the quality and material of the substrate, the ratio between the sizes of the pump spot and the structure, as well as the type of excited mode [33,38]. Since the pump spot does not illuminate the structure fully in this experiment, the number of carriers generated in the local region should be sufficient to compensate for losses in the non-excited part of the structure, which leads to a higher lasing threshold.

The transition from spontaneous to stimulated emission is shown in more detail in Fig. 3. Figure 3(a) illustrates two simultaneously existing trends: (1) the threshold character of the dependence of the total fluorescence intensity on the fluence (S-curve), which experiences a characteristic inflection at $0.57 \text{ mJ}/\text{cm}^2$, and (2) a sharp decrease in the relaxation time of Δn and carriers at the same fluence from over 100 ps to <20 ps.

To describe the ultrafast dynamics of the EHP density N_{EHP} and photon density n_{ph} in the lasing mode disregarding diffusion and

after pump beam arrival, the system of coupled laser rate equations can be used [62–65]:

$$\begin{cases} \frac{\partial N_{\text{EHP}}}{\partial t} = -AN_{\text{EHP}} - BN_{\text{EHP}}^2 - CN_{\text{EHP}}^3 - v_g G n_{\text{ph}} N_{\text{EHP}}, \\ \frac{\partial n_{\text{ph}}}{\partial t} = -v_g \gamma n_{\text{ph}} + \Gamma v_g G n_{\text{ph}} N_{\text{EHP}} + \Gamma \beta B N_{\text{EHP}}^2. \end{cases} \quad (3)$$

Here, A is the trapping rate constant, B is the radiative decay constant, C is the Auger recombination rate constant, v_g is the group velocity, G is the gain coefficient (or “dynamic gain”), γ is the resonator loss, β is the coupling constant, and Γ is the confinement factor of the lasing mode. The fitting results are shown in Figs. 3(b) and 3(c), and the detailed description of the model and the full set of fitting parameters are provided in Supplement 1, Section 3.

Both below the lasing threshold [fluence of $0.35 \text{ mJ}/\text{cm}^2$, purple curve in Fig. 3(b)] and above the lasing threshold [fluence of $0.8 \text{ mJ}/\text{cm}^2$, red curve in Fig. 3(b)], the fitting of the experimental data by the model gives the values of $A = 2 \cdot 10^8 \text{ s}^{-1}$, $B = 1.8 \cdot 10^{-9} \text{ cm}^3/\text{s}$, $C \leq 1 \cdot 10^{-29} \text{ cm}^6/\text{s}$, which are consistent with the literature (Table 1). Auger recombination does not significantly affect the carrier dynamics at the given concentration ($\sim 10^{19} \text{ cm}^{-3}$), and therefore its contribution can be neglected [34].

Fitting of the experimental data is shown in Fig. 3(b) (inset) in logarithmic scale in the case of both lasing and without lasing. Figure 3(c) also shows the detailed carrier dynamics in the first 100 ps after the arrival of the pump pulse. The model makes it possible to describe quantitatively the dynamics of carriers both at times of the order of several picoseconds [Fig. 3(c)] and at subnanosecond scales [Fig. 3(b), inset]. The photon densities n_{ph} obtained as the result of the numerical solution of Eq. (3) are also shown in Fig. 3(c) and agree with the experimental data of other works [45].

To determine the characteristic relaxation times and compare the values obtained with literature data, a simplified biexponential decay model is used [45]. As a result of approximation by the biexponential model $\Delta n = ae^{-t/\tau_{\text{lasing}}} + be^{-t/\tau_{\text{fluor}}}$, the characteristic relaxation times are: $\tau_{\text{lasing}} = 13.4 \pm 1.3 \text{ ps}$ for stimulated emission and $\tau_{\text{fluor}} = 170 \pm 20 \text{ ps}$ for spontaneous emission, which are in good agreement with literature data [34,45].

Finally, we turn to ultrafast spatiotemporal visualization of electron–hole plasma in a perovskite microlaser. The schematic

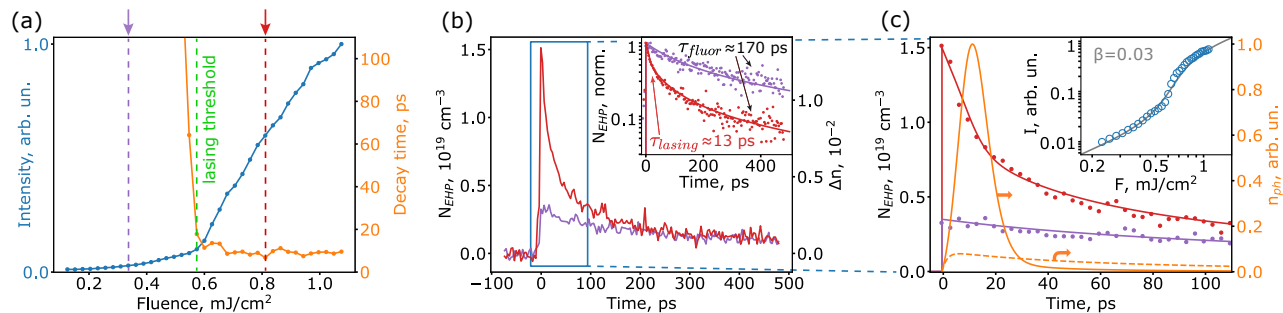


Fig. 3. Ultrafast carrier dynamics during lasing. (a) Dependence of the sample fluorescence intensity (blue) and the relaxation time of the refractive index (orange) on the pump fluence. The green dashed line is the lasing threshold, and the red and purple dashed lines mark the fluences at which the relaxation curves were taken in (b). (b) Relaxation curves of the refractive index and, accordingly, of the EHP density at pump fluences below (purple, $0.35 \text{ mJ}/\text{cm}^2$) and above the lasing threshold (red, $0.8 \text{ mJ}/\text{cm}^2$). The inset illustrates the same curves in a logarithmic scale fitted with Eq. (3). (c) Zoomed area of relaxation curves and their fit for time delays from 0 ps to 100 ps; the dashed and solid orange curves represent the cavity photon density obtained with Eq. (3) for the fluence of $0.35 \text{ mJ}/\text{cm}^2$ (multiplied by 20 for clarity) and $0.8 \text{ mJ}/\text{cm}^2$, respectively. The inset shows the light–light curve [62], which is the dependence of the sample fluorescence intensity on the pump fluence from (a) (blue circles) along with the fitting by Eq. (3) (gray curve), corresponding to the coupling constant $\beta = 0.03$.

of the sample and the generated cloud are shown in Fig. 4(a). The intensity profile of the beam is Gaussian with radius of $2.25\ \mu\text{m}$, which leads to a similar distribution of the free carrier cloud N_{EHP} and refractive index Δn at the moment of arrival of the pump pulse $\tau = 0$ ps.

The generated cloud relaxes as a result of diffusion, as well as stimulated, spontaneous, and nonradiative transitions, which leads to a change in both the amplitude and the shape of the EHP cloud profile [6]. The two-dimensional distribution of the plasma cloud in the first 500 ps after the arrival of the pump pulse is shown in Fig. 4(b); the corresponding plasma distribution cross sections are illustrated in Fig. 4(d). The main relaxation occurs in the first 100 ps after the arrival of the pump pulse due to stimulated radiation. Figure 4(c) shows the detailed ultrafast spatiotemporal dynamics of the electron-hole plasma cloud in the interval from -10 ps to 90 ps in 10 ps steps.

The system of coupled equations Eq. (3) describes the interaction of carriers and photons in the laser mode and yields important characteristics of a microlaser (see Supplement 1, Section 3 for details). However, adding a diffusion term leads to excessive model complexity. To simplify the calculations, it was decided to use the diffusion equation and take into account the interaction of carriers and photons during lasing through a time-dependent coefficient $k_{\text{lasing}}(t)$ (effective stimulated emission coefficient). Thus, to describe the experimental results in Fig. 4, the following equation was used (see Supplement 1, Section 4 for details):

$$\frac{\partial N_{\text{EHP}}}{\partial t} = D \nabla^2 N_{\text{EHP}} - A N_{\text{EHP}} - (k_{\text{lasing}}(t) + k_{\text{fluor}}) N_{\text{EHP}}^2, \quad (4)$$

where $N_{\text{EHP}} = N_{\text{EHP}}(x, y, z, t)$ is the spatial distribution of carrier density in time, D is the diffusion constant, k_{fluor} is the spontaneous emission constant, and ∇ is the nabla operator.

The simulated plasma distribution cross sections are shown in Fig. 4(e). The values of A and $k_{\text{fluor}} = B$ were taken from Eq. (3), and the values of $k_{\text{lasing}}(t)$ and D were used to bring the model into

agreement with the experimental data in Fig. 4(d). Since no diffusion is observed at times up to 500 ps, the model helps to give an upper estimate for the carrier diffusion coefficient: $D \leq 1\ \text{cm}^2/\text{s}$. The value $D = 1.1\ \text{cm}^2/\text{s}$ [61] known for single crystal CsPbBr_3 microplates turns out to be very close to the estimation obtained.

The developed method can also be used to study the carrier diffusion in other nanophotonic devices, for example, in silicon waveguides, for which the diffusion coefficient D is much higher. The determined value of $D = 15\ \text{cm}^2/\text{s}$ is consistent with the literature [7]; see Supplement 1, Section 5 for details. Thus, the perovskite low carrier diffusion coefficient in comparison with other semiconductors is also preserved during lasing. The generated carrier cloud remains localized for at least a nanosecond, which contributes to the high efficiency of lasing and fluorescence of perovskites. To the best of our knowledge, the diffusion coefficient of a perovskite material in the presence of lasing has been estimated for the first time. A comparison of the perovskite microlaser parameters measured by the ultrafast OCM with the data of other works is shown in Table 1.

Thus, the developed method can be used to simultaneously estimate a whole set of basic parameters of a perovskite microlaser: the carrier relaxation rate as the result of spontaneous and stimulated transitions, the threshold value of the carrier concentration for lasing, and the carrier diffusion coefficient. The high spatial and temporal resolutions of the method makes it possible to visualize the relaxation of a plasma cloud in the presence of laser generation.

The advantages of the method, shown on the perovskite sample, can also be applied to study the ultrafast spatiotemporal dynamics of Δn in various nanophotonic devices. The registered Δn can be caused by the generation of free carriers (as in the case of the studied perovskite sample), by the optical Kerr effect (without free carrier generation), and by other processes.

The main current limitation is the sensitivity of the method (10^{-3} RIU), but this value can be further improved using phase stability compensation algorithms [18] and sources with the wider

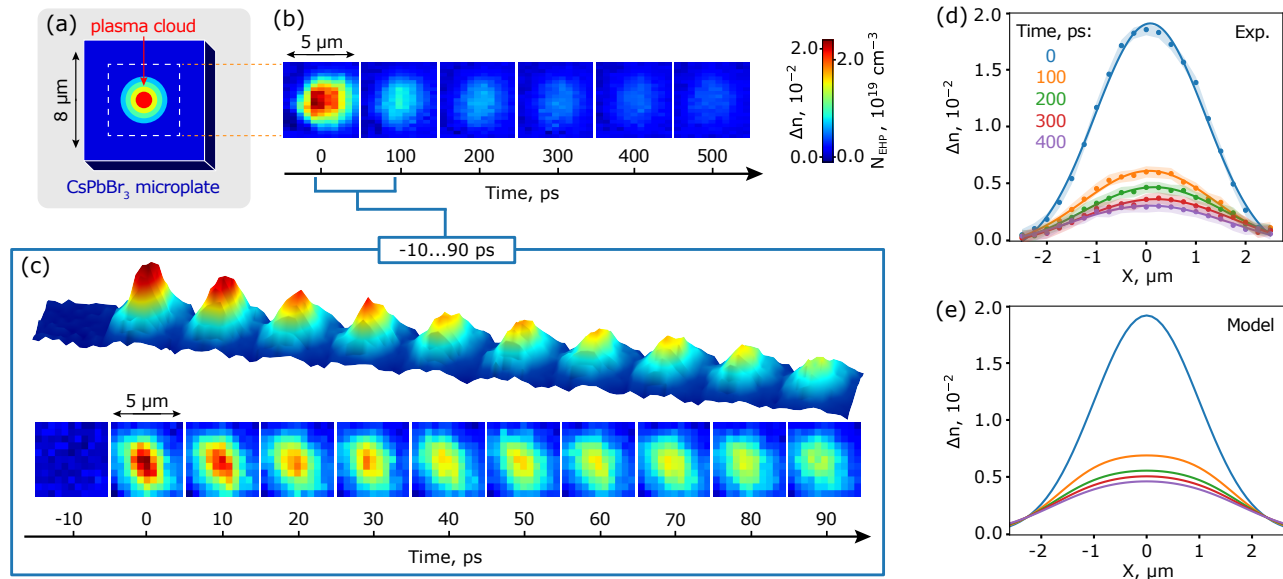


Fig. 4. Ultrafast spatiotemporal dynamics of plasma in a perovskite microcrystal. (a) Schematic of the crystal sample ($8 \times 8\ \mu\text{m}^2$) and generated plasma cloud. The white dashed square marks the scanning area with the OCM beam ($5 \times 5\ \mu\text{m}^2$). (b) Spatiotemporal dynamics of Δn and corresponding N_{EHP} in the first 500 ps after the arrival of the pump pulse. (c) Detailed spatiotemporal plasma dynamics up to the first 90 ps. Color bar is common for (b) and (c). (d) Experimental plasma distribution cross section (dots) fitted by a Gaussian function (curves) for clarity. (e) Corresponding simulated plasma distribution cross section according to Eq. (4).

spectrum. This is especially relevant for thin samples, in which changes in the optical path are small. The temporal resolution can be improved by using wide spectrum ultrashort pulses instead of supercontinuum generation. The limitations on the objects under study include transparency in the sample range (near IR), a flat shape on the waist scale (4.5 μm), as well as the refractive index contrast between the sample and the medium/substrate of at least 0.1 RIU. Limitations can be circumvented by using shorter probe wavelengths in the transparency region of the substrate and sample and high-NA objectives with oil immersion to achieve a smaller waist size, but it should be noted that for CsPbBr_3 perovskites, the Δn (N_{EHP}) dependence in the visible range will have a complex form due to the resonances of materials (see Supplement 1, Section 2). As a result, many nanophotonic devices that perform field localization and free carrier generation, such as microlasers, nonlinear optical waveguides, microcavities, nanoantennas, detectors, and many other objects, including those of integrated silicon photonics, are suitable objects for study.

Given the possibilities and limitations described above, we believe that the developed method of ultrafast OCM is a promising tool for solving many problems of modern nanophotonics, especially when it is necessary to study the dynamics of carriers with both high spatial and high temporal resolutions.

4. CONCLUSIONS

A novel method for ultrafast visualization of refractive index modulation in nanophotonic devices based on optical coherence microscopy combined with the pump–probe scheme is implemented and tested on perovskite microlasers, whose carrier dynamics during lasing is of great interest. The electron–hole plasma spatiotemporal dynamics in a perovskite microcrystal during lasing is successfully visualized with a resolution of 1 ps in time and 0.5 μm in space. The carrier concentration required to start the laser generation is determined to be $1.1 \cdot 10^{19} \text{ cm}^{-3}$ simultaneously with diffusion coefficient $D \leq 1 \text{ cm}^2/\text{s}$, and the decay times of carriers $\tau_{\text{lasing}} = 13 \text{ ps}$, $\tau_{\text{fluor}} = 170 \text{ ps}$. The perovskite carrier diffusion coefficient is low compared to other semiconductors and is found to be maintained during lasing. Therefore, the generated carrier cloud remains localized, which contributes to the high efficiency of lasing and fluorescence. The developed method is promising not only for studying the spatiotemporal dynamics of carriers in microlasers, but also for its further application in the study of the light–matter interaction in various nanophotonic devices and novel photonic materials. This universal approach can solve emerging problems in the rapidly developing field of nanophotonics and expand the scope of OCT-based methods' applications.

Funding. Foundation for the Advancement of Theoretical Physics and Mathematics (BASIS 19-2-6-28-1); Ministry of Education and Science of the Russian Federation; Russian Science Foundation (20-12-00371, optical coherence microscopy measurements).

Acknowledgment. The authors thank Alexander A. Ezhov for the AFM measurements. A.A.P. acknowledges support by the "BASIS" Foundation. S.V.M. and A.P.P. acknowledge the Priority 2030 Federal Academic Leadership Program.

Disclosures. The authors declare no conflicts of interest.

Data availability. Data underlying the results presented in this paper are not publicly available at this time but may be obtained from the authors upon reasonable request.

Supplemental document. See Supplement 1 for supporting content.

REFERENCES

1. Z. Zhou, B. Yin, and J. Michel, "On-chip light sources for silicon photonics," *Light Sci. Appl.* **4**, e358 (2015).
2. B. E. Saleh and M. C. Teich, *Fundamentals of Photonics* (Wiley, 2019).
3. Y. Berdnikov, I. Shtrom, M. Rozhavskaia, W. Lundin, N. Hendricks, R. Grange, and M. Timofeeva, "Mapping of Fabry–Perot and whispering gallery modes in GaN microwires by nonlinear imaging," *Nanotechnology* **32**, 40LT01 (2021).
4. A. Y. Frolov, N. Verellen, J. Li, X. Zheng, H. Paddubrouskaya, D. Denkova, M. R. Shcherbakov, G. A. Vandenbosch, V. I. Panov, P. Van Dorpe, A. A. Fedyanin, and V. V. Moshchalkov, "Near-field mapping of optical Fabry–Perot modes in all-dielectric nanoantennas," *Nano Lett.* **17**, 7629–7637 (2017).
5. A. Y. Frolov, J. Van de Vondel, V. I. Panov, P. Van Dorpe, A. A. Fedyanin, V. V. Moshchalkov, and N. Verellen, "Probing higher order optical modes in all-dielectric nanodisk, -square, and -triangle by aperture type scanning near-field optical microscopy," *Nanophotonics* **11**, 543–557 (2022).
6. M. I. Saidaminov, K. Williams, M. Wei, A. Johnston, R. Quintero-Bermudez, M. Vafaie, J. M. Pina, A. H. Proppe, Y. Hou, G. Walters, S. O. Kelley, W. A. Tisdale, and E. H. Sargent, "Multi-cation perovskites prevent carrier reflection from grain surfaces," *Nat. Mater.* **19**, 412–418 (2020).
7. M. M. Gabriel, J. R. Kirschbrown, J. D. Christesen, C. W. Pinion, D. F. Zigler, E. M. Grumstrup, B. P. Mehl, E. E. Cating, J. F. Cahoon, and J. M. Papanikolas, "Direct imaging of free carrier and trap carrier motion in silicon nanowires by spatially-separated femtosecond pump–probe microscopy," *Nano Lett.* **13**, 1336–1340 (2013).
8. Z. Guo, J. S. Manser, Y. Wan, P. V. Kamat, and L. Huang, "Spatial and temporal imaging of long-range charge transport in perovskite thin films by ultrafast microscopy," *Nat. Commun.* **6**, 7471 (2015).
9. R. Bruck, B. Mills, B. Troia, D. J. Thomson, F. Y. Gardes, Y. Hu, G. Z. Mashanovich, V. Passaro, G. T. Reed, and O. L. Muskens, "Device-level characterization of the flow of light in integrated photonic circuits using ultrafast photomodulation spectroscopy," *Nat. Photonics* **9**, 54–60 (2015).
10. K. Vynck, N. J. Dinsdale, B. Chen, R. Bruck, A. Z. Khokhar, S. A. Reynolds, L. Cradginton, D. J. Thomson, G. T. Reed, P. Lalanne, and O. L. Muskens, "Ultrafast perturbation maps as a quantitative tool for testing of multi-port photonic devices," *Nat. Commun.* **9**, 2246 (2018).
11. L. Wittenbecher, E. Viñas Boström, J. Vogelsang, S. Lehman, K. A. Dick, C. Verdozzi, D. Zigmantas, and A. Mikkelsen, "Unraveling the ultrafast hot electron dynamics in semiconductor nanowires," *ACS Nano* **15**, 1133–1144 (2021).
12. M. Yannai, R. Dahan, A. Goralach, Y. Adiv, K. Wang, I. Madan, S. Gargiulo, F. Barantani, E. J. Dias, G. M. Vanacore, N. Rivera, F. Carbone, F. J. G. de Abajo, and I. Kaminer, "Ultrafast electron microscopy of nanoscale charge dynamics in semiconductors," *ACS Nano* **17**, 3645–3656 (2023).
13. D. Huang, E. A. Swanson, C. P. Lin, J. S. Schuman, W. G. Stinson, W. Chang, M. R. Hee, T. Flotte, K. Gregory, C. A. Puliafito, and J. G. Fujimoto, "Optical coherence tomography," *Science* **254**, 1178–1181 (1991).
14. W. Drexler and J. G. Fujimoto, *Optical Coherence Tomography: Technology and Applications* (Springer, 2015), Vol. 2.
15. D. P. Popescu, L. Choo-Smith, C. Fluerau, Y. Mao, S. Chang, J. Disano, S. Sherif, and M. G. Sowa, "Optical coherence tomography: fundamental principles, instrumental designs and biomedical applications," *Biophys. Rev.* **3**, 155–169 (2011).
16. V. Crecea, B. W. Graf, T. Kim, G. Popescu, and S. A. Boppart, "High resolution phase-sensitive magnetomotive optical coherence microscopy for tracking magnetic microbeads and cellular mechanics," *IEEE J. Sel. Top. Quantum Electron.* **20**, 25–31 (2013).
17. N. M. Israelsen, C. R. Petersen, A. Barh, D. Jain, M. Jensen, G. Hanneschläger, P. Tidemand-Lichtenberg, C. Pedersen, A. Podoleanu, and O. Bang, "Real-time high-resolution mid-infrared optical coherence tomography," *Light Sci. Appl.* **8**, 11 (2019).
18. Y. Li, S. Moon, J. J. Chen, Z. Zhu, and Z. Chen, "Ultrahigh-sensitive optical coherence elastography," *Light Sci. Appl.* **9**, 58 (2020).
19. G. Popescu, Y. Park, W. Choi, R. R. Dasari, M. S. Feld, and K. Badizadegan, "Imaging red blood cell dynamics by quantitative phase microscopy," *Blood Cells Mol. Diseases* **41**, 10–16 (2008).
20. M. A. Sirotni, M. N. Romodina, E. V. Lyubin, I. V. Soboleva, and A. A. Fedyanin, "Single-cell all-optical coherence elastography with optical tweezers," *Biomed. Opt. Express* **13**, 14–25 (2022).

21. J. Czajkowski, T. Prykäri, E. Alarousu, J. Palosaari, and R. Myllylä, "Optical coherence tomography as a method of quality inspection for printed electronics products," *Opt. Rev.* **17**, 257–262 (2010).
22. A. C. Lamont, M. A. Restaino, A. T. Alsharhan, Z. Liu, D. X. Hammer, R. D. Sochol, and A. Agrawal, "Direct laser writing of a titanium dioxide-laden retinal cone phantom for adaptive optics-optical coherence tomography," *Opt. Mater. Express* **10**, 2757–2767 (2020).
23. R. Zvagelsky, F. Mayer, D. Beutel, C. Rockstuhl, G. Gornard, and M. Wegener, "Towards in-situ diagnostics of multi-photon 3D laser printing using optical coherence tomography," *Light Adv. Manuf.* **3**, 466–480 (2022).
24. K. R. Safronov, V. O. Bessonov, D. V. Akhremenkov, M. A. Sirotnin, M. N. Romodina, E. V. Lyubin, I. V. Soboleva, and A. A. Fedyanin, "Miniature Otto prism coupler for integrated photonics," *Laser Photon. Rev.* **16**, 2100542 (2022).
25. M. A. Sirotnin, E. V. Lyubin, K. R. Safronov, D. V. Akhremenkov, V. O. Bessonov, I. V. Soboleva, and A. A. Fedyanin, "Phase-sensitive optical coherence microscopy of integrated nanophotonics devices," *J. Phys. Conf. Ser.* **2015**, 012143 (2021).
26. S. Moon and D. Y. Kim, "Ultra-high-speed optical coherence tomography with a stretched pulse supercontinuum source," *Opt. Express* **14**, 11575–11584 (2006).
27. G. Humbert, W. Wadsworth, S. Leon-Saval, J. Knight, T. Birks, P. St. J. Russell, M. Lederer, D. Kopf, K. Wiesauer, E. Breuer, and D. Stifter, "Supercontinuum generation system for optical coherence tomography based on tapered photonic crystal fibre," *Opt. Express* **14**, 1596–1603 (2006).
28. D. S. S. Rao, M. Jensen, L. Grüner-Nielsen, J. T. Olsen, P. Heiduschka, B. Kemper, J. Schnekenburger, M. Glud, M. Mogensen, N. M. Israelsen, and O. Bang, "Shot-noise limited, supercontinuum-based optical coherence tomography," *Light Sci. Appl.* **10**, 133 (2021).
29. K. D. Rao, M. A. Choma, S. Yazdanfar, A. M. Rollins, and J. A. Izatt, "Molecular contrast in optical coherence tomography by use of a pump-probe technique," *Opt. Lett.* **28**, 340–342 (2003).
30. O. Carrasco-Zevallos, R. L. Shelton, W. Kim, J. Pearson, and B. E. Applegate, "In vivo pump-probe optical coherence tomography imaging in *Xenopus laevis*," *J. Biophoton.* **8**, 25–35 (2015).
31. L. Protesescu, S. Yakunin, M. I. Bodnarchuk, F. Krieg, R. Caputo, C. H. Hendon, R. X. Yang, A. Walsh, and M. V. Kovalenko, "Nanocrystals of cesium lead halide perovskites (CsPbX_3 , X = Cl, Br, and I): novel optoelectronic materials showing bright emission with wide color gamut," *Nano Lett.* **15**, 3692–3696 (2015).
32. A. S. Berestennikov, P. M. Voroshilov, S. V. Makarov, and Y. S. Kivshar, "Active meta-optics and nanophotonics with halide perovskites," *Appl. Phys. Rev.* **6**, 031307 (2019).
33. S. Makarov, A. Furasova, E. Tiguntseva, A. Hemmetter, A. Berestennikov, A. Pushkarev, A. Zakhidov, and Y. Kivshar, "Halide-perovskite resonant nanophotonics," *Adv. Opt. Mater.* **7**, 1800784 (2019).
34. H. Zhu, Y. Fu, F. Meng, X. Wu, Z. Gong, Q. Ding, M. V. Gustafsson, M. T. Trinh, S. Jin, and X. Zhu, "Lead halide perovskite nanowire lasers with low lasing thresholds and high quality factors," *Nat. Mater.* **14**, 636–642 (2015).
35. B. R. Sutherland and E. H. Sargent, "Perovskite photonic sources," *Nat. Photonics* **10**, 295–302 (2016).
36. J. Fan, W. Du, Y. Mi, and X. Liu, "Perovskite-based lasers: an introductory survey," in *Nanoscale Semiconductor Lasers* (Elsevier, 2019), pp. 41–74.
37. A. Vinattieri and G. Giorgi, *Halide Perovskites for Photonics* (AIP, 2021).
38. K. R. Safronov, A. A. Popkova, D. I. Markina, A. P. Pushkarev, S. V. Makarov, V. O. Bessonov, and A. A. Fedyanin, "Efficient emission outcoupling from perovskite lasers into highly directional and long-propagation-length Bloch surface waves," *Laser Photon. Rev.* **16**, 2100728 (2022).
39. M. V. Kovalenko, L. Protesescu, and M. I. Bodnarchuk, "Properties and potential optoelectronic applications of lead halide perovskite nanocrystals," *Science* **358**, 745–750 (2017).
40. J. Chen, D. J. Morrow, Y. Fu, W. Zheng, Y. Zhao, L. Dang, M. J. Stolt, D. D. Kohler, X. Wang, K. J. Czech, M. P. Hautzinger, S. Shen, L. Guo, A. Pan, and J. C. Wright, "Single-crystal thin films of cesium lead bromide perovskite epitaxially grown on metal oxide perovskite (SrTiO_3)," *J. Am. Chem. Soc.* **139**, 13525–13532 (2017).
41. S. Chen and A. Nurmikko, "Excitonic gain and laser emission from mixed-cation halide perovskite thin films," *Optica* **5**, 1141–1149 (2018).
42. A. P. Schlaus, M. S. Spencer, K. Miyata, F. Liu, X. Wang, I. Datta, M. Lipson, A. Pan, and X.-Y. Zhu, "How lasing happens in CsPbBr_3 perovskite nanowires," *Nat. Commun.* **10**, 265 (2019).
43. B. Wu, W. Ning, Q. Xu, M. Manjappa, M. Feng, S. Ye, J. Fu, S. Lie, T. Yin, F. Wang, T. W. Goh, P. C. Harikesh, Y. K. E. Tay, Z. X. Shen, F. Huang, R. Singh, G. Zhou, F. Gao, and T. C. Sum, "Strong self-trapping by deformation potential limits photovoltaic performance in bismuth double perovskite," *Sci. Adv.* **7**, eabd3160 (2021).
44. Y. Gao, J. Liu, F. H. Isikgor, M. Wang, J. I. Khan, S. De Wolf, and F. Laquai, "Probing ultrafast interfacial carrier dynamics in metal halide perovskite films and devices by transient reflection spectroscopy," *ACS Appl. Mater. Interfaces* **14**, 34281–34290 (2022).
45. G. Weng, J. Tian, S. Chen, J. Yan, H. Zhang, Y. Liu, C. Zhao, X. Hu, X. Luo, J. Tao, S. Chen, Z. Zhu, J. Chu, and H. Akiyama, "Electron-hole plasma lasing dynamics in $\text{CsPbCl}_2\text{Br}_3$ -m microplate lasers," *ACS Photon.* **8**, 787–797 (2020).
46. Q. Zhang, S. T. Ha, X. Liu, T. C. Sum, and Q. Xiong, "Room-temperature near-infrared high-Q perovskite whispering-gallery planar nanolasers," *Nano Lett.* **14**, 5995–6001 (2014).
47. Q. Zhang, R. Su, X. Liu, J. Xing, T. C. Sum, and Q. Xiong, "High-quality whispering-gallery-mode lasing from cesium lead halide perovskite nanoplatelets," *Adv. Funct. Mater.* **26**, 6238–6245 (2016).
48. S. D. Stranks, V. M. Burlakov, T. Leijtens, J. M. Ball, A. Goriely, and H. J. Snaith, "Recombination kinetics in organic-inorganic perovskites: excitons, free charge, and subgap states," *Phys. Rev. Appl.* **2**, 034007 (2014).
49. A. P. Pushkarev, V. I. Korolev, D. I. Markina, F. E. Komissarenko, A. Naujokaitis, A. Drabavicius, V. Pakstas, M. Franckevicius, S. A. Khubezhov, D. A. Sannikov, A. V. Zasedatelev, P. G. Lagoudakis, A. A. Zakhidov, and S. V. Makarov, "A few-minute synthesis of CsPbBr_3 nanolasers with a high quality factor by spraying at ambient conditions," *ACS Appl. Mater. Interfaces* **11**, 1040–1048 (2018).
50. J.-H. Cha, J. H. Han, W. Yin, C. Park, Y. Park, T. K. Ahn, J. H. Cho, and D.-Y. Jung, "Photoresponse of CsPbBr_3 and Cs_4PbBr_6 perovskite single crystals," *J. Phys. Chem. Lett.* **8**, 565–570 (2017).
51. M. Liao, B. Shan, and M. Li, "In situ Raman spectroscopic studies of thermal stability of all-inorganic cesium lead halide (CsPbX_3 , X = Cl, Br, I) perovskite nanocrystals," *J. Phys. Chem. Lett.* **10**, 1217–1225 (2019).
52. J. Zhang, X. Lu, L. Sun, Q. Liu, X. Zhao, L. Ma, A. Ge, S. Wang, X. Shen, and W. Lu, "The strain-modulated single-mode laser of perovskite microsheets with grooves on ultrathin flexible mica," *Laser Photon. Rev.* **16**, 2200222 (2022).
53. K.-L. Yan, R.-H. Fan, M. Chen, K. Sun, L.-W. Yin, H. Li, S.-B. Pan, and M.-X. Yu, "Perovskite (La , Sr) MnO_3 with tunable electrical properties by the Sr-doping effect," *J. Alloys Compd.* **628**, 429–432 (2015).
54. Q. Shang, C. Li, S. Zhang, Y. Liang, Z. Liu, X. Liu, and Q. Zhang, "Enhanced optical absorption and slowed light of reduced-dimensional CsPbBr_3 nanowire crystal by exciton-polariton," *Nano Lett.* **20**, 1023–1032 (2020).
55. Q. A. Akkerman, S. G. Motti, A. R. Srimath Kandada, E. Mosconi, V. D'Innocenzo, G. Bertoni, S. Marras, B. A. Kamino, L. Miranda, F. De Angelis, A. Petrozza, M. Prato, and L. Manna, "Solution synthesis approach to colloidal cesium lead halide perovskite nanoplatelets with monolayer-level thickness control," *J. Am. Chem. Soc.* **138**, 1010–1016 (2016).
56. S. Polishchuk, M. Puppini, A. Crepaldi, G. Gatti, D. N. Dirin, O. Nazarenko, N. Colonna, N. Marzari, M. V. Kovalenko, M. Grioni, and M. Chergui, "Nanoscale-resolved surface-to-bulk electron transport in CsPbBr_3 perovskite," *Nano Lett.* **22**, 1067–1074 (2022).
57. A. Hangleiter, Z. Jin, M. Gerhard, D. Kalincev, T. Langer, H. Bremers, U. Rossow, M. Koch, M. Bonn, and D. Turchinovich, "Efficient formation of excitons in a dense electron-hole plasma at room temperature," *Phys. Rev. B* **92**, 241305 (2015).
58. A. Chanana, X. Liu, C. Zhang, Z. V. Vardeny, and A. Nahata, "Ultrafast frequency-agile terahertz devices using methylammonium lead halide perovskites," *Sci. Adv.* **4**, eaar7353 (2018).
59. X. Li, K. Wang, M. Chen, S. Wang, Y. Fan, T. Liang, Q. Song, G. Xing, and Z. Tang, "Stable whispering gallery mode lasing from solution-processed formamidinium lead bromide perovskite microdisks," *Adv. Opt. Mater.* **8**, 2000030 (2020).
60. K. Park, J. W. Lee, J. D. Kim, N. S. Han, D. M. Jang, S. Jeong, J. Park, and J. K. Song, "Light-matter interactions in cesium lead halide perovskite nanowire lasers," *J. Phys. Chem. Lett.* **7**, 3703–3710 (2016).

61. X.-Z. Li, N. Aihemaiti, H.-H. Fang, G.-Y. Huang, Y.-K. Zhou, X.-J. Wang, Y. Zhang, R. Xing, S. Peng, B. Bai, and H.-B. Sun, "Optical visualization of photoexcitation diffusion in all-inorganic perovskite at high temperature," *J. Phys. Chem. Lett.* **13**, 7645–7652 (2022).
62. E. Tiguntseva, K. Koshelev, A. Furasova, P. Tonkaev, V. Mikhailovskii, E. V. Ushakova, D. G. Baranov, T. Shegai, A. A. Zakhidov, Y. Kivshar, and S. V. Makarov, "Room-temperature lasing from Mie-resonant nonplasmonic nanoparticles," *ACS Nano* **14**, 8149–8156 (2020).
63. W. Gao and S. F. Yu, "Reality or fantasy—perovskite semiconductor laser diodes," *EcoMat* **3**, e12077 (2021).
64. Q. Gu and Y. Fainman, *Semiconductor Nanolasers* (Cambridge University, 2017).
65. D. A. Tatarinov, S. S. Anoshkin, I. A. Tsibizov, V. Sheremet, F. Isik, A. Y. Zhizhchenko, A. B. Cherepakhin, A. A. Kuchmizhak, A. P. Pushkarev, H. V. Demir, and S. V. Makarov, "High-quality CsPbBr₃ perovskite films with modal gain above 10 000 cm⁻¹ at room temperature," *Adv. Opt. Mater.* **11**, 2202407 (2023).